An Efficient Control-oriented Modeling Approach for Vibration-prone Delta 3D printers using Receptance Coupling

Nosakhare Edoimioya and Chinedum E. Okwudire

Abstract-Delta 3D printers have the potential to significantly increase throughput in additive manufacturing because they enable faster and more precise motion when compared to traditional serial-axis 3D printers. Further improvements in motion speed and part quality can be realized through model-based feedforward vibration control, as demonstrated on several serial-axis 3D printers. However, delta 3D printers have not benefited from model-based controllers due to their coupled nonlinear dynamics which vary as a function of position. In this paper, we propose a framework to obtain linear models of delta 3D printers as functions of position. We decompose the dynamics into two sub-models: (1) an experimentally-identified sub-model containing decoupled vibration dynamics; and (2) an analytically-derived sub-model containing coupled rigid-body dynamics. These two sub-models are combined into one using receptance coupling. Employing the proposed approach, experiments are used to demonstrate reasonably accurate predictions of the position-dependent vibration dynamics of a delta 3D printer across its workspace using only two frequency response measurements at one location.

I. INTRODUCTION

A delta 3D printer uses three actuators connected in parallel to move the end-effector (nozzle) of the printer. As a result, it boasts higher speeds and accelerations than equivalent 3D printers with serial kinematics [1]. Furthermore, delta 3D printers command identical speeds in all three Cartesian axes, whereas the speed of serial 3D printers vary—with the vertical (z) axis usually having speeds much lower than the lateral (x,y) axes. Accordingly, they have expanded the capabilities of fused filament fabrication (FFF) and, for example, have been shown to improve the quality of Curved Layer FFF [2], which varies the z-axis position within layers, whereas in traditional FFF, the z-axis position is static in each layer.

However, much like serial 3D printers, delta 3D printers experience vibration when they travel at high speeds due to structural flexibilities in their kinematic chain. Modelbased feedforward control techniques have been used to compensate vibration in serial 3D printers, resulting in one order of magnitude increase in achievable acceleration and up to 2x reduction in print time without sacrificing quality [3], [4], [5]. Unfortunately, accurate model-based vibration compensation is challenging for delta 3D printers due to their position-dependent and coupled nonlinear dynamics. One would need accurate models at every location in a delta 3D printer's workspace to accurately compensate its vibration.

The challenge of controlling delta robots due to their complex dynamics is well-documented [6]. It has been

Department of Mechanical Engineering, University of Michigan-Ann Arbor, 2350 Hayward Street, Ann Arbor, MI 48104, USA.

addressed by using various techniques to estimate servo errors, such as sophisticated observers [7], [8] and neural networks [9]. These techniques usually deal with the dynamic variations of delta robots as disturbances which are suppressed using feedback control [10], [11], [12]. However, most commercial delta 3D printers cannot benefit from such approaches because they utilize stepper motors for actuation, which have no feedback sensors. Therefore, they must rely on models that accurately capture their position-dependent coupled dynamics for feedforward vibration compensation.

Receptance coupling is an approach used to combine analytical models and measurements of sub-assemblies of a system, in order to model the full assembly's frequency response function (FRF) [13]. It simplifies modeling by providing flexibility in circumstances where it may be difficult or impossible to obtain measurements that describe the system, such as the position-dependent dynamics of the delta 3D printer. It requires careful selection of sub-assemblies that can be accurately modeled analytically as well as those for which measurements can be easily obtained. Hence, as its primary contributions, this paper:

- Proposes an efficient approach for modeling the position-dependent and coupled dynamics of delta 3D printers that decomposes the printer's dynamics into experimentally-identified vibration dynamics and analytically-derived rigid body dynamics, which are combined via receptance coupling, and
- 2) Demonstrates the effectiveness of the proposed approach on a delta 3D printer by predicting the printer's vibration dynamics at arbitrary locations in its workspace based on only two system identification experiments at one location.

The rest of the paper is as follows: Section II describes the construction of the delta 3D printer and motivates our modeling problem with an example; Section III describes the proposed methodology to decompose the delta model into two sub-models combined to form the full nonlinear dynamic model, which is linearized to obtain a linear parameter varying (LPV) model; Section IV uses a commercial 3D printer as a case study to validate the model's accuracy; and Section V presents our conclusions and future work.

II. BACKGROUND AND MOTIVATION

A. Description of Delta 3D Printer

The three pairs of forearms on the delta 3D printer are connected to a carriage on one end, an end-effector on the other end, and are allowed to rotate freely about universal

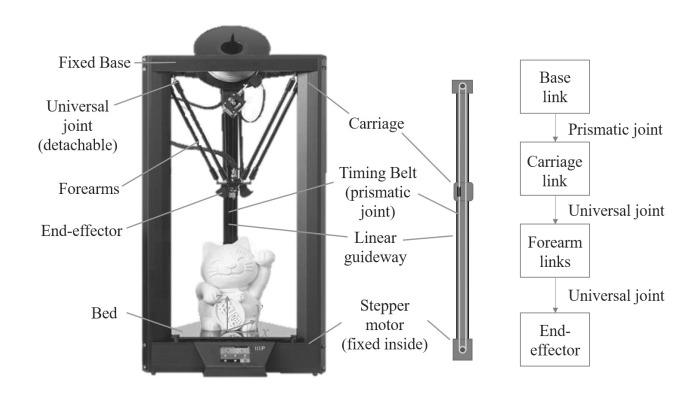


Fig. 1. From left to right: A commercial delta 3D Printer (Monoprice Delta Pro) with labeled components, a schematic of the belt-driven carriage system, and the delta robot configuration showing the connections between joints and links. The print volume dimensions are $270 \times 270 \times 300$ mm.

joints (see Fig. 1). Each carriage translates vertically on linear guideways and is mounted to a timing belt, which is, in turn, connected to a base-mounted stepper motor via a motor pulley, forming a prismatic joint. The relative position of each carriage (i.e., the joint space) determine the Cartesian position of the 3-DOF end-effector (i.e., the task space), which holds a nozzle that heats and deposits melted filament onto a stationary bed. The parallelogram formed by each pair of forearms guarantees that the end-effector and fixed base remain co-planar. In the case of the Monoprice (MP) Delta Pro 3D printer shown in Fig. 1 (as well as several commercial printers), the universal joints are iron balls which allow the magnetized ends of the forearms to be detached and reattached by the user.

As will be discussed in Sec. III, the kinematics of the delta robot are characterized by a set of nonlinear, holonomic spherical constraint equations that relate the task and joint space, such that the motion of one carriage may have an effect on the other carriages and vice versa. As a result, the dynamics of the printer vary from location to location as demonstrated in the following motivational example.

B. Motivational Example

Figure 2 depicts the variability of the FRF from commanded (i.e., desired) to actual position of one carriage, measured with the end-effector at three separate locations of the printer's workspace. These FRFs demonstrate the difficulty in modeling the system through only measurements, as one would have to measure the FRF of all three carriages at several locations to accurately represent the dynamics. Naive modeling of the dynamics with, for example, one measurement may lead to poor vibration compensation due to dynamic variation at other locations. Hence, a simpler and more efficient modeling approach is needed.

III. PROPOSED MODELING APPROACH

We assume that the vibration dynamics of the delta printer is dominated by the spring-mass-damper behavior between the stepper motor, elastic timing belts, and the carriage. Therefore, the vibration dynamics can be lumped at the

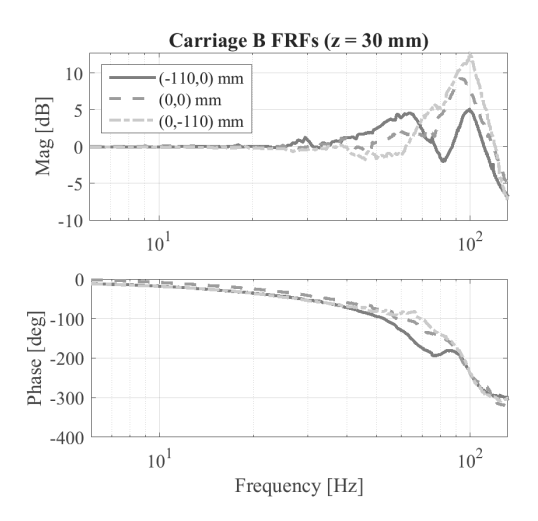


Fig. 2. Motivating example of one carriage's frequency response functions, from commanded to actual position, measured at three different (x,y) locations (all at z=30 mm). This example shows the position varying dynamics and demonstrates the need for a framework for estimating dynamics without having to measure at several locations.

carriage and the exogenous dynamics is dominated by rigid body effects beyond the carriage. Thus, we can decompose the model of the assembly into two sub-models. Sub-model 1 describes the carriage output position q_i as a function of two inputs: the commanded position of the carriage q_{d_i} and the forces F_{q_i} imposed on the carriage due to the end-effector's motion where $i \in \{A, B, C\}$ denotes the carriages labeled A, B, and C (see Fig. 3). Sub-model 2 models the relationship between the end-effector position $\mathbf{X} = [x \ y \ z]^T$ and F_{q_i} .

Sub-model 1 is decoupled and assumed to be linear. The relationships between the inputs and q_i are given by continuous-time linear time invariant (LTI) single input single output (SISO) systems $G_{q_{d_i}}(s)$ and $G_{Fq_i}(s)$, which are measured from experiments (or modeled analytically) as a summation of vibration modes, such that:

$$q_i(s) = G_{q_{d_i}}(s)q_{d_i}(s) + G_{Fq_i}(s)h_i(\mathbf{X}, s)$$
 (1)

where s is the Laplace variable and h_i describes the relationship between \mathbf{X} and F_{q_i} . Note that due to symmetry, we can assume the FRFs are equal for each carriage, i.e., $G_{q_d}(s) = G_{q_d}(s)$ and $G_{Fq_i}(s) = G_{Fq}(s)$ for all i.

Sub-model 2 assumes rigid body motion of the forearms and end-effector, which may include damping, and, for simplicity, neglects the rotation of the forearms [6], [14]. The mass of the forearms are assumed to be split equally between the carriage and the end-effector. The relationship between \mathbf{X} and F_{q_i} are characterized by the Jacobian matrix, which relates the joint space velocities to the task space velocities [6] as

$$\dot{\mathbf{X}} = \mathbf{J}\dot{\mathbf{a}} \tag{2}$$

where $\mathbf{q} = [q_A \quad q_B \quad q_C]^T$ is the joint space coordinate vector, $\mathbf{X} = f(\mathbf{q})$ is the direct-geometric model of the robot, and $\mathbf{J} \in \mathbb{R}^{3 \times 3}$ is the Jacobian matrix, which is composed of partial derivatives of f.

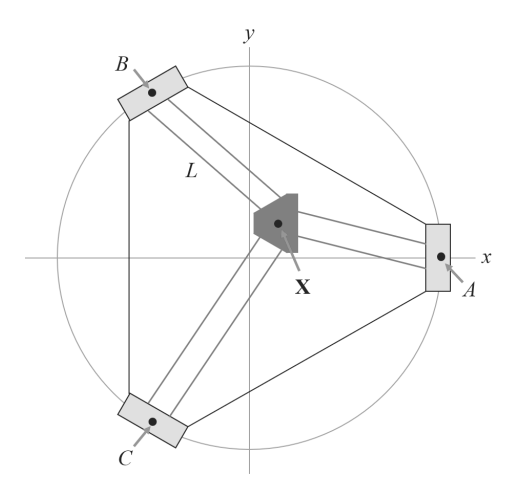


Fig. 3. Overhead view of the delta 3D printer showing the (x,y)-coordinate locations of carriages A, B, and C, the end-effector's location in task space X, and the length of the forearms L.

To derive the Jacobian (based on work from [6]), we assume, without loss of generality, that the origin of the task space coordinate system is located at the center of the bed, the x-axis is aligned with the center of carriage A, and carriages B and C are spaced 120° apart from A (Fig. 3). All six forearms are identical and have length L and we locate \mathbf{X} at the center of the end-effector, on the xy-plane intersecting the forearm/end-effector joints, such that the vertical distance from this plane down to the tip of the hot-end is given by H_{ez} (see Fig. 4). The spherical constraint equations that govern the kinematics are given by

$$(x - A_x)^2 + (y - A_y)^2 + (z + H_{ez} - q_A)^2 = L^2$$
 (3)

$$(x - B_x)^2 + (y - B_y)^2 + (z + H_{ez} - q_B)^2 = L^2$$
 (4)

$$(x - C_x)^2 + (y - C_y)^2 + (z + H_{ez} - q_C)^2 = L^2$$
 (5)

where (A_x, A_y) are the x- and y-axis coordinates of carriage A, (B_x, B_y) are the x- and y-axis coordinates of carriage B and so on. We can write Eqs. 3-5 as

$$\mathbf{s}_i^T \mathbf{s}_i - L^2 = 0 \tag{6}$$

where

$$\mathbf{s}_{i} = \begin{bmatrix} x - i_{x} \\ y - i_{y} \\ z + H_{ez} - q_{i} \end{bmatrix} = \begin{bmatrix} x \\ y \\ z \end{bmatrix} - \left(\begin{bmatrix} i_{x} \\ i_{y} \\ -H_{ez} \end{bmatrix} + \begin{bmatrix} 0 \\ 0 \\ 1 \end{bmatrix} q_{i} \right) \quad (7)$$

Taking the time derivative of Eq. 6 yields

$$\mathbf{s}_i^T \dot{\mathbf{s}}_i + \dot{\mathbf{s}}_i^T \mathbf{s}_i = 0 \tag{8}$$

which, from the commutative property of the vector product, can be rewritten as

$$\mathbf{s}_i^T \dot{\mathbf{s}}_i = 0 \tag{9}$$

where

$$\dot{\mathbf{s}}_{i} = \begin{bmatrix} \dot{x} \\ \dot{y} \\ \dot{z} \end{bmatrix} + \begin{bmatrix} 0 \\ 0 \\ -1 \end{bmatrix} \dot{q}_{i} = \dot{\mathbf{X}} + \mathbf{p}\dot{q}_{i}. \tag{10}$$

Rearranging Eq. 9, with the definition of p, we have

$$\begin{bmatrix} \mathbf{s}_{A}^{T} \\ \mathbf{s}_{B}^{T} \\ \mathbf{s}_{C}^{T} \end{bmatrix} \dot{\mathbf{X}} + \begin{bmatrix} \mathbf{s}_{A}^{T} \mathbf{p} & 0 & 0 \\ 0 & \mathbf{s}_{B}^{T} \mathbf{p} & 0 \\ 0 & 0 & \mathbf{s}_{C}^{T} \mathbf{p} \end{bmatrix} \dot{\mathbf{q}} = \begin{bmatrix} 0 \\ 0 \\ 0 \end{bmatrix}. \tag{11}$$

From Eq. 11, we can obtain the relation in Eq. 2 where

$$\mathbf{J} = -\begin{bmatrix} \mathbf{s}_A^T \\ \mathbf{s}_B^T \\ \mathbf{s}_C^T \end{bmatrix}^{-1} \begin{bmatrix} \mathbf{s}_A^T \mathbf{p} & 0 & 0 \\ 0 & \mathbf{s}_B^T \mathbf{p} & 0 \\ 0 & 0 & \mathbf{s}_C^T \mathbf{p} \end{bmatrix}. \tag{12}$$

After another time derivative of Eq. 11 and some transformations, we find the task space acceleration $\ddot{\mathbf{X}}$ as

$$\ddot{\mathbf{X}} = \begin{bmatrix} \mathbf{s}_A^T \\ \mathbf{s}_B^T \\ \mathbf{s}_C^T \end{bmatrix}^{-1} \begin{pmatrix} \begin{bmatrix} \dot{\mathbf{s}}_A^T \\ \dot{\mathbf{s}}_B^T \\ \dot{\mathbf{s}}_C^T \end{bmatrix} \mathbf{J} + \mathbf{K} \end{pmatrix} \dot{\mathbf{q}} + \mathbf{J} \ddot{\mathbf{q}} = \mathbf{J} \ddot{\mathbf{q}} + \dot{\mathbf{J}} \dot{\mathbf{q}}$$
(13)

where

$$\mathbf{K} = \begin{bmatrix} \dot{\mathbf{s}}_A^T \mathbf{p} & 0 & 0 \\ 0 & \dot{\mathbf{s}}_B^T \mathbf{p} & 0 \\ 0 & 0 & \dot{\mathbf{s}}_C^T \mathbf{p} \end{bmatrix}.$$

The inertial forces in task space are given by

$$\mathbf{F}_e = m_{nt} \ddot{\mathbf{X}} + b_{nt} \dot{\mathbf{X}},\tag{14}$$

respectively, where m_{nt} and b_{nt} are the mass and damping coefficient of the end-effector and forearm assembly, respectively. The contribution of these forces to the joint space can be determined by multiplying them by the transpose of the Jacobian matrix [6]:

$$\Gamma_e = \mathbf{J}^T \mathbf{F}_e = m_{nt} \mathbf{J}^T \ddot{\mathbf{X}} + b_{nt} \mathbf{J}^T \dot{\mathbf{X}}$$

$$= m_{nt} \mathbf{J}^T (\mathbf{J} \ddot{\mathbf{q}} + \dot{\mathbf{J}} \dot{\mathbf{q}}) + b_{nt} \mathbf{J}^T \mathbf{J} \dot{\mathbf{q}}$$
(15)

We can linearize the forces about an equilibrium position denoted by $\bar{\mathbf{X}} = [\bar{x} \ \bar{y} \ \bar{z}]^T$, $\bar{\mathbf{q}} = [\bar{q}_A \ \bar{q}_B \ \bar{q}_C]^T$ such that Γ_e becomes

$$\bar{\Gamma}_e = m_{nt} \bar{\mathbf{J}}^T \bar{\mathbf{J}} \dot{\mathbf{q}} + b_{nt} \bar{\mathbf{J}}^T \bar{\mathbf{J}} \dot{\mathbf{q}}$$
 (16)

where $\bar{\bf J}={\bf J}(\bar{\bf X},\bar{\bf q})$ is the Jacobian evaluated at $\bar{\bf X}$ and $\bar{\bf q}$. Hence, from Eq. 1, we have

$$\mathbf{q}(s) = \mathbf{G}_{q_d}(s)\mathbf{q}_d(s) + \mathbf{G}_{Fq}(s)[m_{nt}s^2 + b_{nt}s]\mathbf{\bar{J}}^T\mathbf{\bar{J}}\mathbf{q}(s)$$
(17)

where $G_{q_d}(s)$ and $G_{Fq}(s)$ are 3×3 diagonal matrices that contain $G_{q_d}(s)$ and $G_{Fq}(s)$, respectively, as diagonal entries.

$$N_{Fq}(s) = m_{nt}s^2 + b_{nt}s \tag{18}$$

then, we can write the coupled dynamics of the combined assembly as

$$\mathbf{q}(s) = \mathbf{G}(s)\mathbf{q}_d(s) \tag{19}$$

where

$$\mathbf{G}(s) = [\mathbf{I} - \mathbf{G}_{Fq}(s)N_{Fq}(s)\bar{\mathbf{J}}^T\bar{\mathbf{J}}]^{-1}\mathbf{G}_{q_d}(s). \tag{20}$$

In Section IV, we present an example where $\mathbf{G}_{q_d}(s)$, $\mathbf{G}_{Fq}(s)$, and $N_{Fq}(s)$ are determined from measurement data at one location and used to predict the FRFs at other locations.

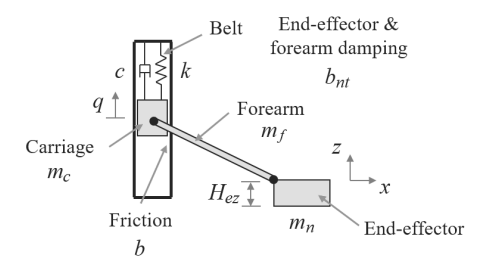


Fig. 4. Modeling schematic for delta 3D printer with the belt-carriage system modeled as a mass-spring-damper system, and the forearm and endeffector modeled as a rigid body mass with a damping coefficient.

IV. EXPERIMENTAL VALIDATION

A. System Identification

The modular nature of commercial delta 3D printers is an advantage in determining the FRFs because we can detach one of the forearms and the end-effector to measure G_{q_d} . For the MP Delta Pro 3D printer, we assume G_{q_d} can be represented (mechanically) as a mass-spring-damper system with stiffness k, belt damping coefficient c, guideway friction b, and mass

$$m = m_c + \frac{1}{2}m_f \tag{21}$$

where m_f is the mass of a pair of forearms and m_c is the lumped mass of the carriage (see Fig. 4).

We obtained the vibration dynamics G_{q_d} , from acceleration data measured using ADXL335 accelerometers on the MP Delta Pro 3D printer. We used a dSPACE MicroLabBox and Pololu stepper motor drivers (DRV8825) to command vertical sine sweep perturbations around ${\bf q}$ corresponding to the task space locations (x,y,z)=(0,0,30),(0,0,50),(0,0,70) mm. Our measurements indicated that G_{q_d} was very similar at the three locations, independent of the z-axis position, so we used data from (0,0,30) mm (see Fig. 5) to fit a 4th-order FRF of the form

$$G_{q_d}(s) = G_{q_{d,m}}(s)G_{q_{d,e}}(s),$$
 (22)

where $G_{q_{d,m}}(s)$ and $G_{q_{d,e}}(s)$ represent the mechanical and electrical dynamics, respectively. The electrical dynamics are created by the electrical circuitry that generates stepper motor commands. Hence, we have

$$G_{q_{d,m}}(s) = \frac{cs+k}{ms^2 + (c+b)s+k}$$
 (23)

$$=\frac{(c/m)s+\omega_n^2}{s^2+2\zeta\omega_ns+\omega_n^2}$$
 (24)

and

$$G_{q_{d,e}}(s) = \frac{d_1 s + d_0}{s^2 + d_2 s + d_0}$$
 (25)

where

$$2\zeta \omega_n = (c+b)/m, \tag{26}$$

$$\omega_n^2 = k/m, \tag{27}$$

and d_0 , d_1 , and d_2 are the coefficients of the electrical FRF. We can obtain the additional equations needed to find c, b,

k, and m by first measuring the mass of the end-effector, m_n , and m_f while the machine is disassembled to obtain

$$m_{nt} = m_n + 3(\frac{1}{2}m_f),$$
 (28)

then reattaching the end-effector assembly and measuring a new carriage FRF at the same location, as shown in Fig. 6. When (x,y)=(0,0), the whole assembly undergoes pure translation. Therefore, we can assume that the added weight and damping from the end-effector is equally distributed to each of the carriages. The measured FRF is also fit with the form of $G_{q_d}(s)$, and the new mechanical FRF is given by:

$$G'_{q_{d,m}}(s) = \frac{cs+k}{m's^2 + b's + k}$$
 (29)

$$= \frac{(c/m')s + \omega_n'^2}{s^2 + 2\zeta'\omega_n's + \omega_n'^2}$$
 (30)

where $m' = m + \frac{1}{3}m_{nt}$, $b' = c + b + \frac{1}{3}b_{nt}$,

$$2\zeta'\omega_n' = b'/m' \tag{31}$$

and

$$\omega_n^{\prime 2} = k/m^{\prime}. \tag{32}$$

From Eqs. 27 and 32, we can determine m as

$$m = \frac{\omega_n'^2}{3(\omega_n^2 - \omega_n'^2)} m_{nt}$$
(33)

which can be used to determine c, b, b_{nt} , and k from the other equations. Table I gives the fitting parameters as well as the identified physical parameters of the delta model. It is also clear in this example that, since all the rigid body parameters are included in $N_{Fq}(s)$,

$$G_{Fq}(s) = -\frac{1}{ms^2 + (c+b)s + k}$$
 (34)

where the negative sign indicates that the forces involved are disturbance forces.

B. Validation

To validate the proposed modeling technique, we use the joint space FRFs identified in Section IV-A to predict the task space FRFs from commanded to output position and compare our predictions with FRFs measured directly in the task space of the MP Delta Pro 3D printer. From Eqs. 2 and 19, we can predict the commanded position to output position FRFs in the task space using the joint space FRFs:

$$\mathbf{X}(s) = \bar{\mathbf{J}}\mathbf{G}(s)\mathbf{q}_d(s) = \bar{\mathbf{J}}\mathbf{G}(s)\bar{\mathbf{J}}^{-1}\mathbf{X}_d(s)$$
(35)

where \mathbf{X}_d is the commanded end-effector position.

Using the predicted dynamics and Eq. 35, we discovered task space locations where the end-effector's FRFs are expected to vary from the FRFs at the origin. We found that (x,y) = (-110,0) and (0,-110) mm showed significant variation for the x-to-x and y-to-y FRFs, respectively. To verify our model, we measured the same FRFs on the MP Delta Pro 3D printer. Figures 7-9 show the predicted and measured FRF comparison for the x-, y-, and z-axis, respectively. When the task space is at the origin, the modes

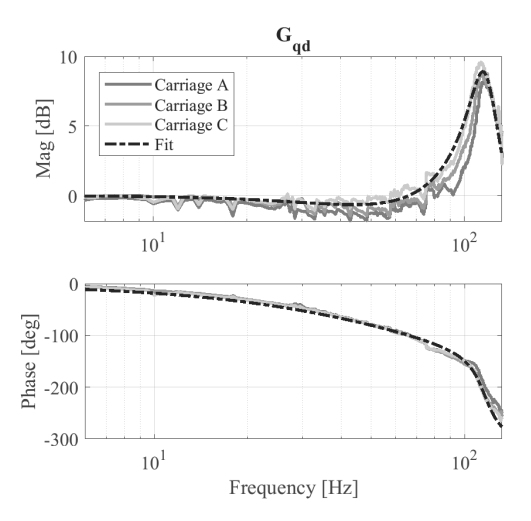


Fig. 5. Position-to-position frequency response functions of the carriage without the end-effector dynamics, G_{q_d} . The data was measured for each carriage at the carriage locations (q_A,q_B,q_C) corresponding to (x,y,z)=(0,0,30) mm, and a linear fit of one of the of the frequency response functions shown as the black dashed line.

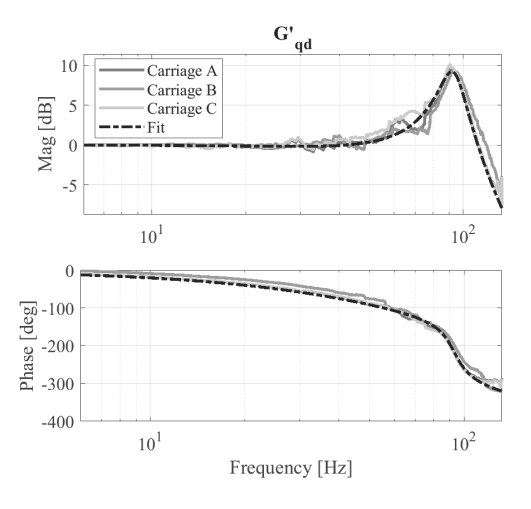


Fig. 6. Position-to-position frequency response functions of the carriage with the end-effector mass, G_{qd}' . The data was measured for the same carriage locations as Figure 5.

TABLE I
System Identification Parameters

Symbol	Value (units)				
m	0.177 kg				
m_n	0.156 kg				
m_f	0.032 kg				
C	5.87 N-s/m				
b	18.0 N-s/m				
b_{nt}	27.9 N-s/m				
k	$9.44 \times 10^4 \text{ N/m}$				
ω_n	730 rad/s				
ω'_n	601 rad/s				
ζ	0.092				
ζ'	0.10				
d_0	$1.43 \times 10^5 \text{ s}^{-2}$				
d_1	-212.1 s^{-1}				
d_2	36.2 s^{-1}				

 $\label{thm:table II}$ Goodness of fit between predicted and measured FRFs

R^2	(x,y) = (0,0) mm		(-110,0) mm		(110,0) mm	
	mag.	phase	mag.	phase	mag.	phase
x-to-x y-to-y z-to-z	0.841 0.763 0.909	0.988 0.996 0.991	0.746 0.866 0.203	0.999 0.996 0.992	0.812 0.621 0.156	0.981 0.999 0.996

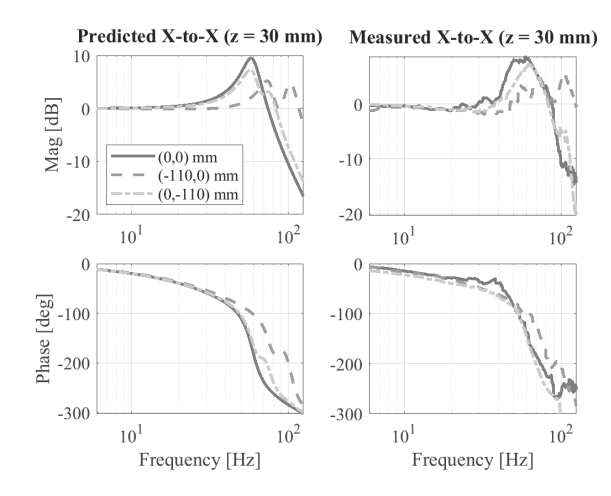


Fig. 7. Frequency response functions of the *x*-to-*x* position at (x,y) = (0,0), (-110,0), and (0,-110) (z = 30 mm for all) predicted with the linearized joint space frequency response functions (left) and measured at the endeffector of the Monoprice Delta Pro 3D printer (right).

from each of the three carriages sum to form one mode in the task space FRFs. But as the end-effector is moved from the origin, the modes of each carriage separate as reflected in the multiple modes in the task space FRFs.

Table II reports the goodness of fit between the measured and predicted FRFs using the coefficient of determination, R^2 , defined as

$$R^{2} = 1 - \frac{\sum_{j} (\nu_{j} - g_{j})^{2}}{\sum_{j} (\nu_{j} - \bar{\nu})^{2}}$$
 (36)

where j is the frequency, v_i are the measured data, \bar{v} is the mean of the measured data across all frequencies, which is used as the baseline model, and g_i are the data from the predicted model, which is compared to the baseline. The R^2 value can be thought of as the proportion of the variance in the measured FRFs that is captured by the predicted FRFs. The mean R^2 of the magnitude and phase of the measured FRFs are 0.657 and 0.993, respectively. The proposed LPV model captures high proportions of the dynamic variations in the xy-plane. The model also captures z-axis magnitude and phase variations close to the task space origin. From Fig. 9, we note that far from the origin the shape of the z-axis magnitudes are similar, but the frequency of the resonance peaks differs by about 10 Hz which decreases the R^2 value. Overall, the model provides reasonably accurate approximations of the measured FRFs, particularly in the x and y directions which are critical for high-speed motion in traditional FFF 3D printing.

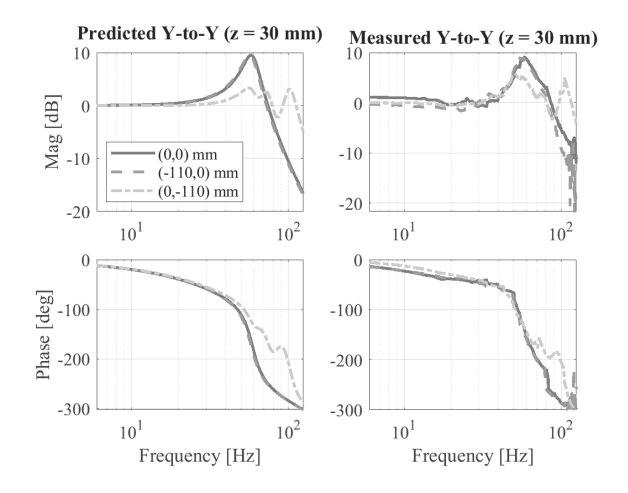


Fig. 8. Frequency response functions of the *y*-to-*y* position at (x,y) = (0,0), (-110,0), and (0,-110) mm, predicted (left) and measured (right).

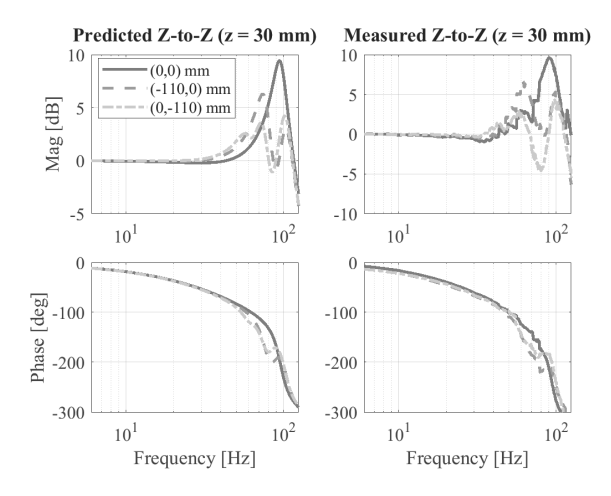


Fig. 9. Frequency response functions of the *z*-to-*z* position at (x,y) = (0,0), (-110,0), and (0,-110), predicted (left) and measured (right).

V. CONCLUSION & FUTURE WORK

The delta 3D printer offers the potential for higher precision and throughput compared to traditional serial-axis 3D printers. However, it has not benefited from the modelbased feedforward vibration compensation methods that have improved the accuracy and speed of serial 3D printers because of the delta's nonlinear dynamics that vary as a function of position. Identifying accurate models of the delta printer was previously difficult because measurements were needed at several locations in the printer's workspace. In this paper, we propose an efficient framework to identify linear models for delta 3D printers using two measurements from only one location. The framework decomposes the dynamics into two sub-models, an experimentally-identified sub-model and an analytically-derived sub-model, and combines them using receptance coupling. We demonstrate the modeling approach using a commercial delta 3D printer and show that the resulting LPV model captures the position-dependent dynamic variations with reasonable accuracy, particularly in the xy-plane which is critical for high-speed control in FFF.

Our modeling framework is presented in the context of model-based feedforward vibration control of the delta 3D printer which cannot use the feedback controllers proposed in the literature due to the lack of feedback sensors. However, the approach is general and can be used in conjunction with feedback techniques to further improve tracking controllers.

In the future, we plan to implement a model-based controller on the delta 3D printer using the model derived in this paper. Given the host of model-based control techniques available, creative utilization of our model with a controller that can effectively exploit its ability to capture dynamic variations may lead to significant improvements in speed and precision in additive manufacturing using the delta robot.

ACKNOWLEDGMENT

This work was supported in part by the National Science Foundation [grant number DGE 1256260] and a Michigan NASA Space Grant Consortium fellowship.

REFERENCES

- K. Miller, "Experimental verification of modeling of delta robot dynamics by direct application of Hamilton's principle," in *International Conference on Robotics and Automation (ICRA)*, pp. 532-37, 1995.
- [2] R.J.A. Allen and R.S. Trask, "An experimental demonstration of effective Curved Layer Fused Filament Fabrication utilizing a parallel deposition robot," *Additive Manufacturing* vol. 8, pp. 78-87, 2015.
- [3] M. Duan, D. Yoon, and C.E. Okwudire, "A limited-preview filtered B-spline approach to tracking control – with application to vibrationinduced error compensation of a 3D printer," *Mechatronics* vol. 56, pp. 287-296, 2018.
- [4] H. Kim and C.E. Okwudire, "Simultaneous servo error precompensation and feedrate optimization with tolerance constraints using linear programming," *International Journal of Advanced Manufacturing Technology*, vol. 109, no. 3-4, pp. 809-821, 2020.
- [5] C.E. Okwudire, S. Huggi, S. Supe, C. Huang, and B. Zeng, "Low-level control of 3D printers from the cloud: a step toward 3D printer control as a service," *Inventions*, vol. 3(3), no. 56, 2018.
- [6] A. Codourey, "Dynamic modeling of parallel robots for computed-torque control implementation," *International Journal of Robotics Research*, vol. 17, no. 18, pp. 1325-1336, 1998.
- [7] M. Ramirez-Neria, H. Sira-Ramírez, A. Luviano-Juárez, and A. Rodrguez-Ángeles, "Active disturbance rejection control applied to a delta parallel robot in trajectory tracking tasks," *Asian Journal of Control*, vol. 17, no. 2, pp. 636-647, 2015.
- [8] L.A. Castañeda, A. Luviano-Juárez, and I. Chairez, "Robust trajectory tracking of a delta robot through adaptive active disturbance rejection control," *IEEE Transactions on Control Systems Technology*, vol. 23, no. 4, pp. 1387-98, 2015.
- [9] J.M. Escorcia-Hernandez, H. Aguilar-Sierra, O. Aguilar-Mejia, A. Chemori, and J.H. Arroyo-Nunez, "An intelligent compensation through B-spline neural network for a delta parallel robot," in *International Conference on Control, Decision and Information Technologies (CoDIT)*, pp. 361-366, 2019.
- [10] L. Angel, J. Viola, "Fractional order PID for tracking control of a parallel robotic manipulator type delta," ISA Transactions, vol. 79, pp. 172-88, 2018.
- [11] C.E. Boudjedir, D. Boukhetala, and M. Bouri, "Nonlinear PD plus sliding mode control with application to a parallel delta robot," *Journal* of Electrical Engineering, vol. 69, no. 5, pp. 329-336, 2018.
- [12] Y. Su, D. Sun, L. Ren, and J.K Mills, "Integration of saturated PI synchronous control and PD feedback for control of parallel manipulators," *IEEE Transactions on Robotics*, vol. 22, no. 1, pp. 202-207, 2006.
- [13] T. Burns and T.L Schmitz, "Receptance coupling study of toollength dependent dynamic absorber effect," in ASME International Mechanical Engineering Congress and Exposition (IMECE), pp. 993-1000, 2004
- [14] Z. Ji, "Study of the effect of leg inertia in Stewart platforms," in International Conference on Robotics and Automation (ICRA), pp. 121-126, 1993.